Research Article Vol. 3, No. 4/25 August 2025/Optica Quantum 381

OPTICA QUANTUM

Quantum teleportation of a silicon nanophotonic CNOT gate

Kai-Chi Chang,[1,†,*] Xiang Cheng,[1,5,†] Felix Ribuot-Hirsch,[1] Murat Can Sarihan,[1] Yujie Chen,[1,6] Jaime Gonzalo Flor Flores,[1] Mingbin Yu,[2,3] Patrick Guo-Qiang Lo,[2,4] Dim-Lee Kwong,[2] and Chee Wei Wong[1,7]

[1]Fang Lu Mesoscopic Optics and Quantum Electronics Laboratory, Department of Electrical and Computer Engineering, University of California, Los Angeles, California 90095, USA
[2]Institute of Microelectronics, Singapore 117685, Singapore
[3]State Key Laboratory of Functional Materials for Informatics, Shanghai Institute of Microsystem and Information Technology and Shanghai Industrial Technology Research Institute, Shanghai 200050, China
[4]Advanced Micro Foundry, Singapore 117685, Singapore
[5]chengxiang@ucla.edu
[6]yujiechen0724@ucla.edu
[7]cheewei.wong@ucla.edu
[†]These authors contributed equally to this work.
*uclakcchang@ucla.edu

Received 1 January 2025; revised 30 June 2025; accepted 21 July 2025; published 7 August 2025

Large-scale quantum computers possess the capacity to effectively tackle practical problems that can be insurmountable for classical computers. The main challenge in building these quantum computers is to realize scalable modules for remote qubits and entanglement. By assembling small, specialized parts into a larger architecture, the modular approach mitigates complexity and uncertainty. Such a distributed architecture requires non-local quantum gate operations between remote qubits. An essential method for implementing such operations, known as quantum gate teleportation, requires only local operations, classical communication, and shared entanglement. Till today, the quantum gate teleportation using a photonic chip has remained elusive. Here, we experimentally demonstrate the quantum teleportation of an on-chip controlled-NOT (CNOT) gate, implemented via a silicon polarization directional coupler. Assisted with the scalable silicon chip platform, high-fidelity local quantum logic gates, linear optical components, post-selected entanglement, and coincidence measurements from photonic qubits, we first measure and characterize our teleported chip-scale CNOT gate with an average truth table fidelity of 93.1 ± 0.3%. Second, for different input polarization states, we obtain an average quantum state fidelity of 87.0 ± 2.2% with our teleported on-chip CNOT gate. Third, we use our non-local CNOT gate for remote entanglement creation of four Bell states, with an average quantum state fidelity of 86.2 ± 0.8%. Fourth, we fully characterize our teleported on-chip CNOT gate with a quantum process fidelity of 83.1 ± 2.0%, and an average non-local CNOT gate fidelity of 86.5 ± 2.2%. Our teleported photonic on-chip quantum logic gate could be extended both to multiple qubits and chip-scale modules towards fault-tolerant and large-scale distributed quantum computation.

© 2025 Optica Publishing Group under the terms of the Optica Open Access Publishing Agreement.

https://doi.org/10.1364/OPTICAQ.554577

1. INTRODUCTION

The quantum advantage of non-classical machines requires coherent manipulation of a large number of qubits [1–9]. As the system size grows, the average physical distance between qubits increases, making it harder to perform high-fidelity logical operations among connected arbitrary qubits. To tackle this problem, quantum state teleportation has been proposed and realized in different physical systems [10–16]. Teleporting quantum logic gate operations is more complex than state teleportation due to higher communication overhead. Implementing a two-qubit gate via state teleportation requires two EPR entangled qubits, four classical bits, and local operations [10,16–19]. In contrast, quantum gate teleportation enables non-local gates between distant qubits, using shared EPR entanglement to avoid direct quantum interaction [10,16–22]. This key solution enables a modular approach to large-scale quantum computing [23–27], because the small and spatially separated processors with available qubits can be arbitrarily connected with quantum links to carry out more complicated computations. Such a quantum network approach has provided practical scaling methods for

several promising candidate systems for the implementation of quantum computation, e.g., in photonic systems [20–22,28], trapped-ion platforms [29–32], and in superconducting hardware [33]. All of these prior works demonstrated the CNOT gate teleportation, owing to its capability to entangle remote qubits [34–44], and such a two-qubit gate has been proven to play a crucial role in entanglement distillation and purification [45–48]. The two-qubit CNOT gate, when combined with single-qubit gates, enables the generation of a highly entangled state for one-way quantum computing [49–57]. Recently, high-fidelity CNOT operation has been developed using silicon on-chip platforms [34,35,39,41]. Such integrated silicon photonics are one of the building blocks for scalable and complex quantum circuits [8,26,27,49,50]. For example, with the complementary metal-oxide-semiconductor (CMOS)-compatible silicon chip-scale platform, high-density photonic integration involving different degree-of-freedoms has been realized [8,26,27], with intrinsic good phase stability and compactness. Although the photonic quantum state teleportation has been demonstrated on-chip [58], and from one chip to another chip [59], however, to the best of our knowledge, the quantum gate teleportation using a silicon nanophotonic chip is lacking.

Here, we experimentally realize a teleported on-chip CNOT gate between two remote nodes using a shared EPR pair of photonic qubits. This demonstration combines key elements for non-local quantum logic gate with flying qubits, including a CMOS-compatible silicon chip, linear optical manipulations, and high-fidelity local quantum logic gates, and the assistance of post-selected entanglement generation and coincidence counting measurements. Here, we teleport a local on-chip CNOT gate, which acts on polarization and path qubits of two local qubits, to a non-local CNOT gate, acting on polarization qubits of two remote qubits. First, we employ non-local truth table measurements to describe our teleported chip-scale CNOT gate, with an average gate fidelity of 93.1 ± 0.3%. Second, we obtain an average fidelity of 87.0 ± 2.2% for various polarization states using our teleported chip-scale CNOT gate. In the third step, our non-local CNOT gate is utilized to remotely create entanglement for all four Bell states, yielding an average quantum state fidelity of 86.2 ± 0.8%. Finally, we comprehensively characterize the logical quantum process of our on-chip CNOT gate through teleported measurements, revealing a complete quantum process fidelity of 83.1 ± 2.0%. Therefore, we demonstrate the quantum teleportation of a chip-scale CNOT gate, exhibiting a mean gate fidelity of 86.5 ± 2.2%, averaged across various input states. Our on-chip CNOT gate device has a size of 50 × 50 μm^2, which is promising for replacing bulky free-space optics components with CMOS integration technology; this could further increase the number of connected modules and qubits for distributed quantum computation. The imperfect teleported on-chip CNOT gate fidelity can possibly be improved by further increasing the finite polarization-extinction ratio in the silicon chip-scale CNOT gate, and the entanglement quality of the photon-pair source. Our teleported on-chip CNOT gate operation can be incorporated into a larger modularized quantum computer that is distributed through optical fibers over longer distances.

2. RESULTS

2.1. Silicon Chip CNOT Gate Teleportation Realization

A distributed quantum computer relies on a network of local nodes that establish communication with each other in both quantum and classical channels (Fig. 1(a)). Each node represents a compact quantum processor comprising two finely optimized subsystems. Now we have two parties, Alice and Bob, each having two qubits 1, 2 and 3, 4, each with quantum information. We have a shared EPR state $|\Phi\rangle_{23} = (|00\rangle_{23} + |11\rangle_{23})/\sqrt{2}$ between the qubits 2 and 3, facilitating interactions between modules by acting as communicators. Each module functions independently as a local node, capable of executing intra-module operations proficiently. Inter-module operations between the two entities are made possible by distributing entanglement among the communication qubits. As a consequence of the isolation between modules, traditional approaches relying on direct quantum interactions cannot be employed to implement multi-qubit operations in the network architecture. Instead, quantum state teleportation is developed for this purpose [10,12–19]. This protocol relies on shared entanglement as a valuable resource, along with deterministic local operations and classical communication between two systems. The combination of these elements forms the distinctive characteristics of teleportation-based protocols, where information is transmitted through quantum and classical channels. Building upon this technique, quantum gate teleportation achieves a unitary gate operation between two unknown states, eliminating the requirement for direct interaction between non-local qubits [10,16]. First, we explain the core concept of non-local gate operations on a photonic platform. The input state of qubits 1 and 4 can be expressed as: $|\Psi\rangle_{14} = A_1|00\rangle + A_2|01\rangle + A_3|10\rangle + A_4|11\rangle$. Let A_1 to A_4 represent normalization values. Next, we carry out deterministic local gate operations on qubits 1 and 2, as well as on qubits 3 and 4. Utilizing the shared EPR entanglement between qubits 2 and 3, along with classical communication, we can teleport a local gate from qubits 1 and 2 to the remote qubits 1 and 4 through the following process:

$$C_{34}C_{12}\left(|\Psi\rangle_{14}\otimes|\Phi\rangle_{23}\right) = |0+\rangle_{23}\otimes C_{14}|\Psi\rangle_{14} + |0-\rangle_{23}\otimes\left(\sigma_1^Z\right)C_{14}|\Psi\rangle_{14} + |1+\rangle_{23}\otimes\left(\sigma_4^X\right)C_{14}|\Psi\rangle_{14} + |1-\rangle_{23}\otimes\left(-\sigma_1^Z\sigma_4^X\right)C_{14}|\Psi\rangle_{14}.$$

As in Fig. 1(a), each node in the network holds a pair of qubits, and qubits 2 and 3 share an entangled state. The state $|\pm\rangle_3 = (|0\rangle_3 \pm |1\rangle_3)/\sqrt{2}$, while C_{34} and C_{12} denote Bob and Alice's CNOT gate operations on qubits 3 and 4, and 1 and 2, respectively. The notation subscripts here are for the different qubits. Here, σ_1^Z and σ_4^X represent Pauli operators acting on the respective qubits. First, we apply a CNOT gate on the local qubits 3 and 4 in the basis $\{|0\rangle_2, |1\rangle_2\}$. Next, qubits 2 and 3 are measured on the basis $\{|+\rangle_3, |-\rangle_3\}$. Depending on the measurement results, we perform one of the following single-bit corrections: $\{I, \sigma_1^z, \sigma_4^X, -\sigma_1^z\sigma_4^X\}$ on remote qubits 1 and 4, enabling the teleportation of a non-local CNOT gate. Via this method, a CNOT gate applied locally to qubits 1 and 2 (C_{12}) can be effectively teleported, resulting in an equivalent operation on distant qubits 1 and 4 (C_{14}). This approach minimizes the classical communication cost compared to standard quantum state teleportation protocols [10,16–22].

In this work, we realize the quantum teleportation of our photonic silicon chip-scale CNOT gate. To achieve efficient chip-scale polarization splitting, a waveguide-to-waveguide gap width of 400 nm and a coupling length of 11.5 μm are implemented. The waveguides are optimized with a thickness of 220 nm silicon for C-band operation. Figure 1(b) is the optical micrograph of the on-chip CNOT gate (size of 50 × 50 μm^2, excluding edge couplers) by the integrated silicon nanophotonic

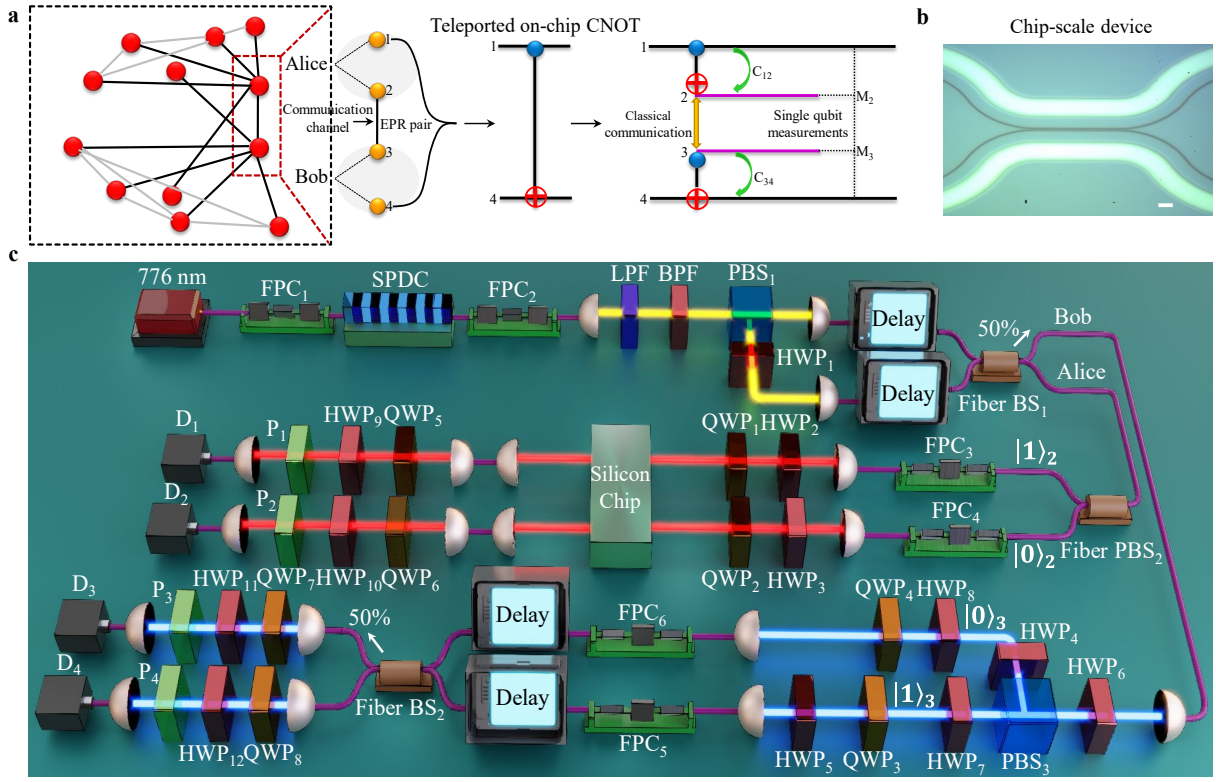

Fig. 1. Quantum teleportation of an on-chip CNOT gate realization scheme. (a) Network overview of the distributed quantum computation. Alice and Bob each have two-qubit (1 to 4, in red circles), sharing an EPR pair between them. Coupling between Alice and Bob is generated through a communication channel. Their two-qubit comprises of a photonic quantum processor that is capable of high-fidelity operations among data qubits (1 and 4) and communication qubits (2 and 3). We then show the teleported CNOT logic between Alice and Bob, which requires (1) EPR entanglement between qubits 2 and 3 (orange arrow), (2) CNOT operations (green arrows: C_{12} and C_{34}), (3) Single-qubit measurement of qubits 2 and 3 in proper basis (M_2 and M_3), and (4) classical communication between Alice and Bob. (b) Optical micrograph of the on-chip CNOT gate by the integrated silicon photonics polarization directional coupler. Scale bar: 2 μm. (c) Experimental setup for quantum teleportation of an on-chip CNOT gate, which includes three main parts, 1. The post-selected polarization entanglement generation; 2. The chip-scale CNOT gate prepared for teleportation in Alice; 3. The free-space two-qubit setup prepared by Bob for teleporting Alice's on-chip CNOT logic operation. $|0\rangle_2$, $|1\rangle_2$, $|0\rangle_3$, and $|1\rangle_3$ are for the notation of path qubits after post-selected polarization entanglement generation. Our integrated CNOT gate is a silicon waveguide device realized by a polarization directional coupler. BPF, Band-pass filter; BS, beam-splitter; D, detector; FPC, fiber polarization controller; HWP, half-wave plate; LPF, long-pass filter; P, linear polarizer; PBS, polarization beam-splitter; QWP, quarter-wave plate; TCSPC, time-correlated single-photon counting.

directional coupler. For the nanofabrication details of our on-chip CNOT gate, see Methods section in Supplement 1. The classical characterization measurements for this chip are provided in our prior work [60].

To successfully implement the experimental demonstration of teleporting our chip-scale CNOT gate, two key requirements must be met: preparing the resource for standard teleportation and enabling the execution of CNOT gates on local qubits. In our physical implementation, we leverage the advantages of the photonic platform, utilizing highly coherent and controllable components. Our measurement setup is presented in Fig. 1(c). With the type-II spontaneous parametric down-conversion (SPDC) process, photon pairs are generated in a post-selected polarization-entangled EPR state $(|HV\rangle + |VH\rangle)/\sqrt{2}$, where $|H\rangle$ and $|V\rangle$ stand for two orthogonal linear polarizations (details in Methods section of Supplement 1). Then, we use two polarization beam-splitters (fiber PBS_2 and free-space PBS_3) to produce individually controllable path qubits for Alice and Bob, respectively. We assign the two paths after PBS_2 as $|0\rangle$ and $|1\rangle$, respectively. We use a fiber polarization controller (FPC_3) and a half-wave plate (HWP_4) to change the polarization from $|V\rangle$ to $|H\rangle$. By doing so, we can transfer the polarization-entanglement to path-entanglement with the whole quantum state expressed as: $|\Psi\rangle_{1234} = |H\rangle_1 \left[\left(|00\rangle_{23} + |11\rangle_{23}\right)/\sqrt{2}\right] |H\rangle_4$, where Alice and Bob carry qubits 1 and 2 and 3 and 4, for the two-qubit CNOT gate operations, respectively. Alice's CNOT gate C_{12} is achieved by our on-chip silicon device, while Bob's CNOT gate C_{34} is realized in a free-space balanced Mach–Zehnder interferometer. For details of the experimental Alice and Bob's CNOT gates, see Methods section in Supplement 1. Subsequently, we prepare arbitrary polarization input states between remote qubits 1 and 4 to implement the quantum teleportation of an on-chip CNOT gate operation.

2.2. Teleported Chip-Scale CNOT Gate Truth Table and Quantum State Tomography

Before performing the non-local CNOT gate protocol, first we measure and optimize the spectral, temporal, and polarization characteristics of our photon-pair source. By carefully sweeping the pump wavelength, we measure that our SPDC source has an ≈0.2-nm center-wavelength difference, operating at

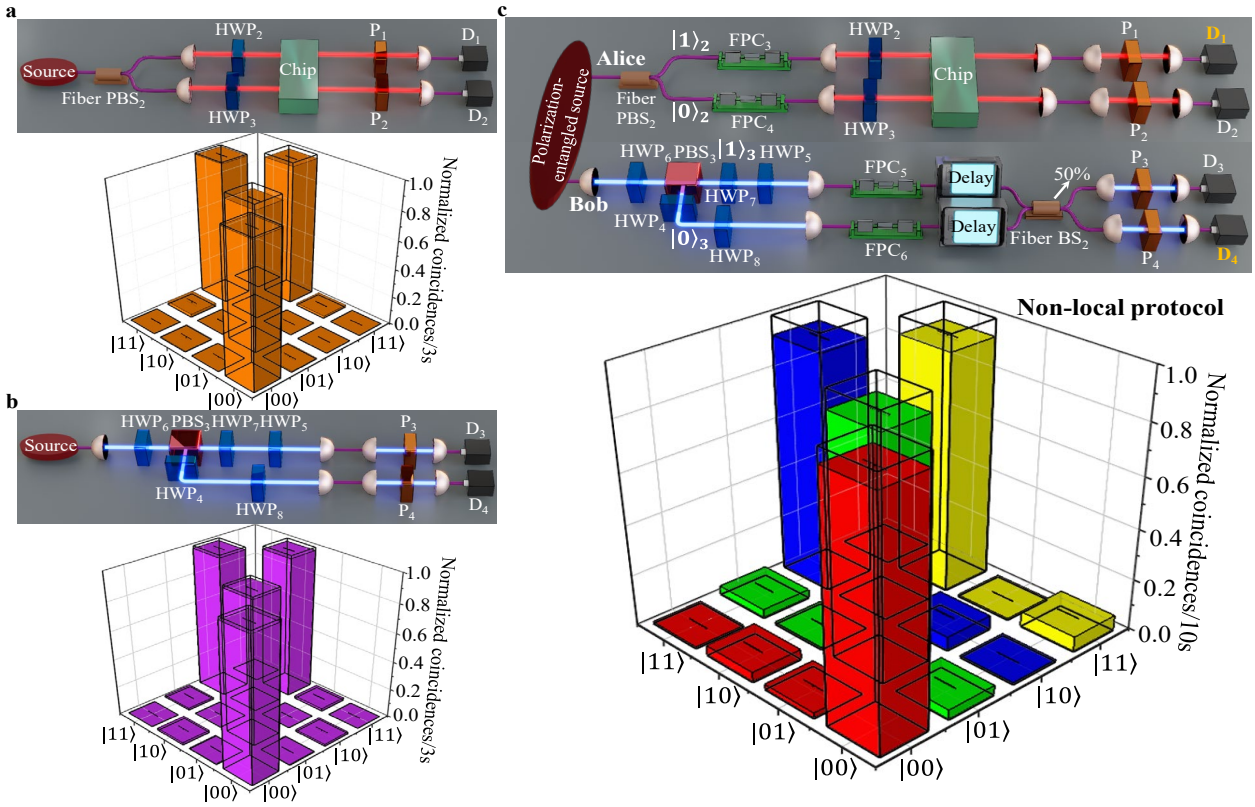

Fig. 2. Teleported truth table of an on-chip CNOT gate and CNOT truth tables from Alice and Bob. (a) Simplified experimental setup (detail in Fig. 1(c)) for truth table measurements of a chip-scale CNOT gate. Alice's CNOT gate has an average gate fidelity of 97.9 ± 0.3%. (b) Free-space CNOT gate truth table and its measurement setup. Bob's CNOT gate has an average gate fidelity of 98.1 ± 0.3%. Errors are given as black ranges and indicate the standard deviations in our measurements. In (a) and (b), errors are given as black ranges and indicate the standard deviations in our measurement, and the expected output states for an ideal CNOT gate are shown as transparent bars. (c) Schematic experimental setup for non-local truth table measurements between detectors 1 and 4 (highlighted in orange color). Below is the non-local protocol for teleporting a chip-scale CNOT gate. The non-local CNOT gate has an average truth table fidelity of 93.1 ± 0.3%. Errors are given as black ranges and indicate the standard deviations in our measurement. The expected output states for an ideal CNOT gate are shown as transparent bars. All the experimental data here are obtained without subtracting accidental coincidences.

near-degenerate conditions. We then proceed to measure the Hong-Ou-Mandel (HOM) two-photon interference [61,62] to characterize our photon-pair source. We obtain a HOM visibility of 97.4 (92.2) ± 0.8% after (before) background subtraction. We also use HOM interference dip to confirm that the path lengths in our free-space Mach–Zehnder interferometer are balanced. After these measurements, we generate polarization-entanglement via post-selection, with 98.5 (93.9) ± 1.0% fringe visibility after (before) background subtraction. For polarization fringes after accidental subtraction, we obtain $S = 2.686 \pm 0.033$ to violate the classical limit by more than 20 standard deviations [35]. All these results are presented in Figures S.1 to S.3 of Supplement 1. We next measure the truth tables for Alice and Bob's CNOT gates as illustrated in Figs. 2(a) and 2(b). For our chip-scale CNOT gate, we directly prepare and send SPDC photons into dual input–output coupling systems, and insert a pair of half-wave plates (HWP_2 and HWP_3) on both input ports before the chip to prepare the $|H\rangle$ ($|0\rangle$) and $|V\rangle$ ($|1\rangle$) polarizations. We use two linear polarizers (P_1 and P_2) before output collimators to perform projection polarization measurements. In Fig. 2(a), on Alice's side, the on-chip CNOT gate has an average gate fidelity of 97.9 ± 0.3%. As for the free-space CNOT gate truth table measurements, we use the SPDC source, remove the FPC_5, FPC_6, two fiber tunable delay lines, fiber BS_2, and connect the outputs of the free-space CNOT gate directly to the two fiber benches. Input polarization states $|H\rangle$ ($|0\rangle$) and $|V\rangle$ ($|1\rangle$) can be prepared with HWP_7 and HWP_8 (while the HWP_5 is fixed at 45° to act as a Bob's CNOT gate), and output polarization projection measurements are done with mounted polarization analyzers (P_3 and P_4). For Fig. 2(b), Bob's CNOT gate has an average gate fidelity of 98.1 ± 0.3%. We note that the average fidelities of our polarization-spatial CNOT gates reported here are comparable to those achieved in a recent demonstration of frequency-polarization CNOT gate [63]. In both Figs. 2(a) and 2(b), errors are given as black ranges and indicate the standard deviations in our measurement, and the expected output states for an ideal CNOT gate are shown as transparent bars. All the experimental data here are obtained without subtracting accidental coincidences.

With the successful demonstration of all the essential elements required for the implementation of the teleported on-chip CNOT gate, we proceeded to thoroughly characterize the non-local two-qubit chip-scale gate through a series of four analyses. In the following, we define the physical qubits $|H\rangle$, $|V\rangle$, $|D\rangle$, $|R\rangle$ in the logical basis as $|0\rangle$, $|1\rangle$, $|+\rangle = (|0\rangle + |1\rangle)/\sqrt{2}$, and $|i\rangle = (|0\rangle + i|1\rangle)/\sqrt{2}$, respectively. In the first analysis, we

confirmed the functionality of the non-local gate by measuring quantum truth tables for the complete set of computational basis states. We prepared the input qubits for all four states $|00\rangle$, $|01\rangle$, $|10\rangle$, and $|11\rangle$ and operated the teleported chip-scale CNOT on them. Figure 2(c) is the experimental teleported truth table of our on-chip CNOT gate. To assess the fidelity of the measured teleported CNOT truth table compared to the ideal one, we performed a calculation that quantifies the degree of similarity between the two: $F = (1/4)\, Tr\left(\frac{M_{exp}M_{ideal}{}^{T}}{M_{ideal}M_{ideal}{}^{T}}\right)$, where M_{exp} and M_{ideal} are the truth tables for the experiment and ideal cases, respectively. Here we optimized and obtained an average truth table fidelity F of 93.1 ± 0.3%. We note that the deviation from unity teleported fidelity arises from our chip-scale CNOT's finite polarization-extinction ratio, the coupling difference between the $|H\rangle$ and $|V\rangle$ states, imperfections from free-space CNOT gate, slight mismatch between signal and idler wavelength that causes non-ideal HOM interference visibility, and polarization-entanglement quality (detailed in Figures S.1 to S.3 in Supplement 1). Errors are given as black ranges and indicate the standard deviations in our measurement. The expected output states for an ideal CNOT gate are shown as transparent bars. All the data are obtained without subtracting accidental coincidences. The results obtained in this analysis offer initial qualitative verification of the teleported chip-scale CNOT gate's performance.

Subsequently, in the second step, we employ quantum state tomography to analyze the on-chip CNOT gate teleportation between remote qubits 1 and 4 (see Supplement 1 for more details), given different input states composed of $|0\rangle$, $|1\rangle$, $|+\rangle$, and $|i\rangle$. The quantum state fidelity can be expressed as: $F_s = \left(Tr\left(\sqrt{\sqrt{\rho_{mea}}\rho_{ideal}\sqrt{\rho_{mea}}}\right)\right)^2$, where ρ_{mea} and ρ_{ideal} are the measured and ideal density matrices, respectively. We represent all of the different input polarization states' reconstructed density matrices in Figures S.4 to S.7 in Supplement 1. Overall, we measure and achieve an average quantum state fidelity of 87.0 ± 2.2% for 14 different input polarization states, namely, $|00\rangle$, $|01\rangle$,$|0+\rangle$, $|0i\rangle$, $|10\rangle$, $|11\rangle$, $|1+\rangle$, $|1i\rangle$, $|++\rangle$, $|+i\rangle$, $|i0\rangle$, $|i1\rangle$, $|i+\rangle$, and $|ii\rangle$ (the other 2 input polarization states $|+0\rangle$, $|+1\rangle$ are presented in the third analysis) with our teleported chip-scale CNOT gate. In addition to the errors stemming from imperfect experimental non-local truth table, these quantities encompass imperfections related to logical state preparation and decoding operations. The ideal values are indicated as transparent bars in the plots. Our quantum state tomography results in Supplement 1 are consistent with our non-local truth table measurements in Fig. 2(c), further confirming the non-local gate operation between remote qubits 1 and 4 using our teleported chip-scale CNOT gate.

2.3. Generation of Logical Bell States and Quantum Process Tomography of an On-Chip CNOT Gate Teleportation

After verifying the non-local CNOT operation with our truth table and quantum state tomography measurements, we proceed to characterize its unique entangling properties. In our third analysis, we represent the unique quantum nature of our teleported on-chip gate by successfully creating entanglement between two distant logical qubits. To achieve this, we initialize the input remote qubits in the separable initial state $|+0\rangle$, $|+1\rangle$, $|-0\rangle$, and $|-1\rangle$ and perform the non-local gate operation, respectively.

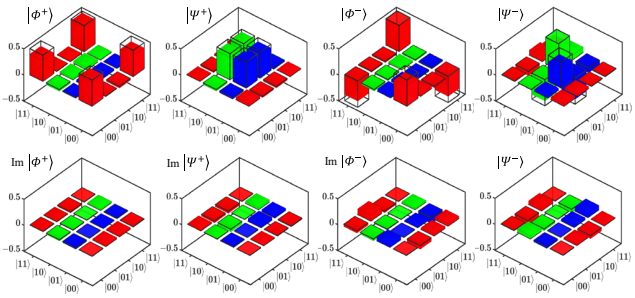

Fig. 3. Reconstructed density matrices for the generated Bell states after a chip-scale CNOT gate teleportation. Produced Bell states after an on-chip CNOT gate teleportation. We show both the real and imaginary parts of the reconstructed density matrices for four Bell states with four different input polarization states of (a) $|+0\rangle$, (b) $|+1\rangle$, (c) $|-0\rangle$, and (d) $|-1\rangle$, respectively. The output states are measured by 16 different output combinations of $|0\rangle$, $|1\rangle$, $|+\rangle$, and $|i\rangle$. For these produced Bell states using a teleported on-chip CNOT gate, we achieve an average quantum state fidelity of 86.2 ± 0.8%. The transparent bars indicate the ideal density matrices for the maximally entangled Bell states.

Their ideal output state corresponds to four Bell states $|\Phi^+\rangle$, $|\Psi^+\rangle$, $|\Phi^-\rangle$, and $|\Psi^-\rangle$, respectively. We express the four maximally entangled Bell states as $|\Phi^\pm\rangle = (|00\rangle \pm (|11\rangle)/\sqrt{2}$, and $|\Psi^\pm\rangle = (|01\rangle \pm (|10\rangle)/\sqrt{2}$. We note that the input polarization states of $|+0\rangle$, $|+1\rangle$, combining with the other 14 polarization states in Supplement 1, form a complete quantum state tomography measurements using $|0\rangle$, $|1\rangle$, $|+\rangle$, and $|i\rangle$ input states. Figures 3(a)–3(d) are the real and imaginary parts of the reconstructed density matrices for all four generated Bell states $|\Phi^+\rangle$, $|\Psi^+\rangle$, $|\Phi^-\rangle$, and $|\Psi^-\rangle$ via our chip-scale CNOT gate teleportation. For these produced Bell states using a teleported on-chip CNOT gate, we achieve an average quantum state fidelity F_s of 86.2 ± 0.8%. The transparent bars indicate the ideal density matrices for the maximally entangled Bell states. The duration of coincidence counting for each experimental data in Fig. 3 is 10 seconds, and all the data are obtained without subtracting accidental coincidences. This recording duration is chosen to have enough coincidence counts for reconstructing the quantum state and process tomography. Our results here confirm the non-local entangling functionality of our teleported chip-scale CNOT gate.

In the fourth analysis, we fully characterize the quantum logical process of the teleported on-chip CNOT gate. To implement this, we conduct a quantum process tomography on the two remote qubits. For an ideal quantum process tomography of a CNOT gate, we depict the real and imaginary parts of the quantum process using the Pauli basis. In this representation, X, Y, and Z correspond to the Pauli matrices σ_X, σ_Y, and σ_Z, respectively. To ensure a quality quantum logical process tomography for our teleported chip-scale CNOT gate, our approach focuses on optimizing each density matrix of the quantum state tomography by carefully selecting appropriate input and output states. In this study, we employ a total of 256 measurement settings to perform a comprehensive quantum process tomography. The fidelity of the quantum process can then be expressed as: $F_p = \left(Tr\left(\sqrt{\sqrt{\chi_{exp}}\chi_{ideal}\sqrt{\chi_{exp}}}\right)\right)^2$, where χ_{exp} and χ_{ideal} are the experimental and ideal process matrices, respectively. From the experimental reconstruction, we extract a process fidelity F_p

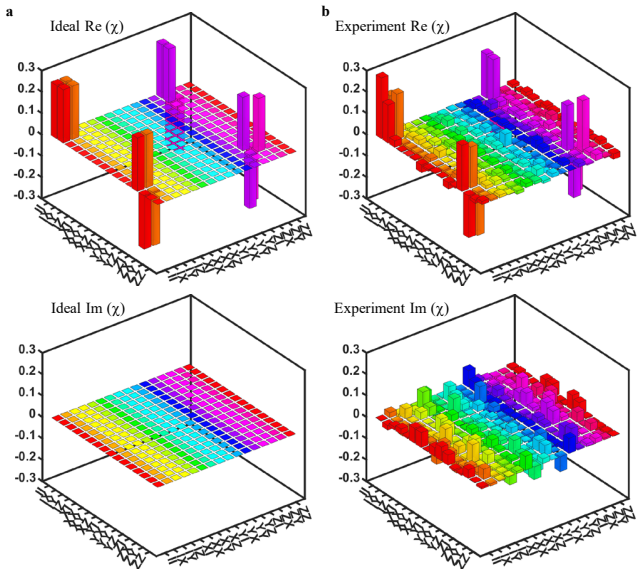

Fig. 4. Teleported quantum process tomography of an on-chip CNOT gate. (a) Ideal quantum process tomography of the CNOT gate. We represent both the real and imaginary parts of quantum process tomography of CNOT gate in the Pauli transfer representation; here, X, Y, and Z are the Pauli matrices σ_X, σ_Y, and σ_Z, respectively. (b) Experimental reconstructed quantum process tomography of a teleported chip-scale CNOT gate. The teleported on-chip CNOT gate process fidelity is measured to be 83.1 ± 2.0%, which corresponds to the average teleported on-chip CNOT gate fidelity of 86.5 ± 2.2%. Agreement between the experimentally reconstructed (Fig. 4(b)) and ideal (Fig. 4(a)) processes indicates the successful implementation of an on-chip CNOT gate teleportation.

of 83.1 ± 2.0%. By using a relation between the quantum process fidelity F_p and the average gate fidelity F_{avg}, with $F_{avg} = \frac{dF_p+1}{d+1}$, and $d = 4$ [34], we obtain an average teleported on-chip CNOT gate fidelity F_{avg} of 86.5 ± 2.2% without subtracting accidental coincidences. The successful implementation of on-chip CNOT gate teleportation is confirmed by the agreement between the experimentally reconstructed process (Fig. 4(b)) and the ideal process (Fig. 4(a)). Our work here provides an important step towards achieving distributed quantum computation in a chip-scalable platform using photonic qubits.

3. CONCLUSION

In summary, we have demonstrated quantum gate teleportation with our integrated silicon chip device, linear optical operations, local quantum logic gates, shared EPR entanglement, and post-selected coincidence measurements in a photonic platform. The quality of our teleported chip-scale CNOT gate is first characterized through non-local truth table measurements with an average gate fidelity of 93.1 ± 0.3%. In the second analysis, we achieve an average quantum state fidelity of 87.0 ± 2.2% for different polarization states after our non-local CNOT gate operation. Third, we perform quantum state tomography to analyze the generation of logical Bell states after an on-chip CNOT gate teleportation, with an average quantum state fidelity of 86.2 ± 0.8%. Finally, we fully characterize the quantum logical process of our teleported on-chip CNOT gate with a quantum process fidelity of 83.1 ± 2.0%. We therefore demonstrate the first teleportation of the chip-scale CNOT gate operation with a mean gate fidelity of 86.5 ± 2.2%, averaged over all the different input states. With recent progress on integrated silicon devices, the extinction ratio of the integrated polarization directional coupler can be further improved, enhancing the local gate fidelity of the on-chip CNOT gate towards higher fidelity non-local photonic gate operations. Moreover, it is possible to further integrate our silicon directional couplers with on-chip waveplates as a monolithic device. Such a device can have similar polarization control accuracy and precision as free-space optics [64]. The integration of several operations in quantum gate teleportation, including CMOS-compatible silicon chips, high-fidelity quantum logic gates, and efficient generation and manipulation of photonic qubits in optical links, will be essential for building large-scale quantum computers based on entangled photons. The protocol employed in our work for the teleported on-chip CNOT gate is one example from a broad range of two-qubit operations that can be achieved utilizing similar resources. These non-local quantum logic gates play a crucial role as fundamental building blocks for modular architectures. Our future endeavors will involve demonstrating non-local chip-to-chip gate teleportation, necessitating remote entanglement between photonic qubits in the telecommunication band. Additionally, our protocol can leverage other approaches, such as deterministic [8,22,30,31,33] and fault-tolerant [9,32] schemes, and can benefit from entanglement purification protocols [47,48]. When combined with non-destructive measurement schemes [65–69], our current implementation has the potential for future adaptation to incorporate more intricate schemes that generate deterministic remote entanglement. Such advancements will be crucial for achieving a scalable and modular qubit architecture.

Funding. Army Research Office (W911NF-21-2-0214); National Science Foundation (QII-TAQS 1936375, QuIC-TAQS 2137984).

Acknowledgment. The authors acknowledge discussions with Sophi Chen Song, Hsiao-Hsuan Chin, and discussions on the superconducting nanowire single-photon detectors with Vikas Anant. This study is supported by the Army Research Office Multidisciplinary University Research Initiative (W911NF-21-2-0214) and the National Science Foundation (QII-TAQS 1936375 and QuIC-TAQS 2137984). K.-C.C. developed the idea. K.-C.C. and X.C. designed the experiments. K.-C.C., X.C., F.R.-H., and Y.C. conducted the measurements. K.-C.C., F.R.-H., and J.G.F.F. contributed to the data analysis. M.C.S. performed the design and simulation of the device. M.Y., P.G-.Q.L., and D.-L.K. performed the device nanofabrication. X.C., F.R.-H., M.C.S., and C.W.W. supported and discussed the studies. K.-C.C., X.C., Y.C., and C.W.W. prepared the manuscript. All authors contributed to the discussion of the manuscript.

Disclosures. The authors declare no conflicts of interest.

Data availability. All data needed to evaluate the conclusions in the paper are present in the paper. Additional data related to this paper may be requested from the authors.

Supplemental document. See Supplement 1 for supporting content.

REFERENCES

1. J. Zhang, G. Pagano, P. W. Hess, *et al.*, "Observation of a many-body dynamical phase transition with a 53-qubit quantum simulator," Nature **551**(7682), 601–604 (2017).
2. F. Arute, K. Arya, R. Babbush, *et al.*, "Quantum supremacy using a programmable superconducting processor," Nature **574**(7779), 505–510 (2019).

3. L. S. Madsen, F. Laudenbach, M. F. Askarani, *et al.*, "Quantum computational advantage with a programmable photonic processor," Nature **606**(7912), 75–81 (2022).
4. J. M. Arrazola, V. Bergholm, K. Brádler, *et al.*, "Quantum circuits with many photons on a programmable nanophotonic chip," Nature **591**(7848), 54–60 (2021).
5. A. J. Daley, I. Bloch, C. Kokail, *et al.*, "Practical quantum advantage in quantum simulation," Nature **607**(7920), 667–676 (2022).
6. H. Y. Huang, M. Broughton, J. Cotler, *et al.*, "Quantum advantage in learning from experiments," Science **376**(6598), 1182–1186 (2022).
7. H.-S. Zhong, H. Wang, Y. H. Deng, *et al.*, "Quantum computational advantage using photons," Science **370**(6523), 1460–1463 (2020).
8. J. Bao, Z. Fu, T. Pramanik, *et al.*, "Very-large-scale integrated quantum graph photonics," Nat. Photonics **17**(7), 573–581 (2023).
9. D. Bluvstein, S. J. Evered, A. A. Geim, *et al.*, "Logical quantum processor based on reconfigurable atom arrays," Nature **626**(7997), 58–65 (2024).
10. X. M. Hu, Y. Guo, B. H. Liu, *et al.*, "Progress in quantum teleportation," Nat. Rev. Phys. **5**(6), 339–353 (2023).
11. W. Luo, L. Cao, Y. Shi, *et al.*, "Recent progress in quantum photonic chips for quantum communication and internet," Light Sci. Appl. **12**(1), 175 (2023).
12. S. L. N. Hermans, M. Pompili, H. K. C. Beukers, *et al.*, "Qubit teleportation between non-neighbouring nodes in a quantum network," Nature **605**(7911), 663–668 (2022).
13. N. Fiaschi, B. Hensen, A. Wallucks, *et al.*, "Optomechanical quantum teleportation," Nat. Photonics **15**(11), 817–821 (2021).
14. X. M. Hu, C. Zhang, B. H. Liu, *et al.*, "Experimental high-dimensional quantum teleportation," Phys. Rev. Lett. **125**(23), 230501 (2020).
15. Y. H. Luo, H. S. Zhong, M. Erhard, *et al.*, "Quantum teleportation in high dimensions," Phys. Rev. Lett. **123**(7), 070505 (2019).
16. S. Pirandola, J. Eisert, C. Weedbrook, *et al.*, "Advances in quantum teleportation," Nat. Photonics **9**(10), 641–652 (2015).
17. M. A. Nielsen and I. L. Chuang, "Programmable quantum gate arrays," Phys. Rev. Lett. **79**(2), 321–324 (1997).
18. D. Gottesman and I. L. Chuang, "Demonstrating the viability of universal quantum computation using teleportation and single-qubit operations," Nature **402**(6760), 390–393 (1999).
19. E. Knill, R. Laflamme, and G. J. Milburn, "A scheme for efficient quantum computation with linear optics," Nature **409**(6816), 46–52 (2001).
20. X. Liu, X.-M. Hu, T.-X. Zhu, *et al.*, "Nonlocal photonic quantum gates over 7.0 km," Nat. Commun. **15**(1), 8529 (2024).
21. W. B. Gao, A. M. Goebel, C. Y. Lu, *et al.*, "Teleportation-based realization of an optical quantum two-qubit entangling gate," Proc. Natl. Acad. Sci. **107**(49), 20869–20874 (2010).
22. Y. F. Huang, X. F. Ren, Y. S. Zhang, *et al.*, "Experimental teleportation of a quantum controlled-NOT gate," Phys. Rev. Lett. **93**(24), 240501 (2004).
23. E. Pelucchi, G. Fagas, I. Aharonovich, *et al.*, "The potential and global outlook of integrated photonics for quantum technologies," Nat. Rev. Phys. **4**(3), 194–208 (2021).
24. W. Bogaerts, D. Pérez, J. Capmany, *et al.*, "Programmable photonic circuits," Nature **586**(7828), 207–216 (2020).
25. J. Wang, F. Sciarrino, A. Laing, *et al.*, "Integrated photonic quantum technologies," Nat. Photonics **14**(5), 273–284 (2020).
26. J. Wang, S. Paesani, Y. Ding, *et al.*, "Multidimensional quantum entanglement with large-scale integrated optics," Science **360**(6386), 285–291 (2018).
27. X. Qiang, X. Zhou, J. Wang, *et al.*, "Large-scale silicon quantum photonics implementing arbitrary two-qubit processing," Nat. Photonics **12**(9), 534–539 (2018).
28. X. Sun, Y. Wang, Y. Tian, *et al.*, "Deterministic and universal quantum squeezing gate with a teleportation-like protocol," Laser Photonics Rev. **16**(3), 2100329 (2022).
29. L. Postler, S. Heußen, I. Pogorelov, *et al.*, "Demonstration of fault-tolerant universal quantum gate operations," Nature **605**(7911), 675–680 (2022).
30. S. Daiss, S. Langenfeld, S. Welte, *et al.*, "A quantum logic gate between distant quantum-network modules," Science **371**(6529), 614–617 (2021).
31. Y. Wan, D. Kienzler, S. D. Erickson, *et al.*, "Quantum gate teleportation between separated qubits in a trapped-ion processor," Science **364**(6443), 875–878 (2019).
32. A. Reiserer, N. Kalb, G. Rempe, *et al.*, "A quantum gate between a flying optical photon and a single trapped atom," Nature **508**(7495), 237–240 (2014).
33. K. S. Chou, J. Z. Blumoff, C. S. Wang, *et al.*, "Deterministic teleportation of a quantum gate between two logical qubits," Nature **561**(7723), 368–373 (2018).
34. L. T. Feng, M. Zhang, X. Xiong, *et al.*, "Transverse mode-encoded quantum gate on a silicon photonic chip," Phys. Rev. Lett. **128**(6), 060501 (2022).
35. M. Zhang, L. Feng, M. Li, *et al.*, "Supercompact photonic quantum logic gate on a silicon chip," Phys. Rev. Lett. **126**(13), 130501 (2021).
36. J. Zeuner, A. N. Sharma, M. Tillmann, *et al.*, "Integrated-optics heralded controlled-NOT gate for polarization-encoded qubits," npj Quantum Inf. **4**, 13 (2018).
37. X.-L. Wang, Y.-H. Luo, H.-L. Huang, *et al.*, "18-Qubit entanglement with six photons' three degrees of freedom," Phys. Rev. Lett. **120**(26), 260502 (2018).
38. S. M. Wang, Q. Q. Cheng, Y. X. Gong, *et al.*, "A 14×14 μm^2 footprint polarization-encoded quantum controlled-NOT gate based on hybrid waveguide," Nat. Commun. **7**(1), 11490 (2016).
39. L.-T. Feng, M. Zhang, Z.-Y. Zhou, *et al.*, "On-chip coherent conversion of photonic quantum entanglement between different degrees of freedom," Nat. Commun. **7**, 11985 (2016).
40. A. Crespi, R. Ramponi, R. Osellame, *et al.*, "Integrated photonic quantum gates for polarization qubits," Nat. Commun. **2**, 566 (2011).
41. A. Politi, M. J. Cryan, J. G. Rarity, *et al.*, "Silica-on-silicon waveguide quantum circuits," Science **320**(5876), 646–649 (2008).
42. C. Fang, Y. Wang, S. Huang, *et al.*, "Crosstalk suppression in individually addressed two-qubit gates in a trapped-ion quantum computer," Phys. Rev. Lett. **129**(24), 240504 (2022).
43. M. Fiorentino and F. N. C. Wong, "Deterministic controlled-NOT gate for single-photon two-qubit quantum logic," Phys. Rev. Lett. **93**(7), 070502 (2004).
44. J. L. O'Brien, G. J. Pryde, A. G. White, *et al.*, "Demonstration of an all-optical quantum controlled-NOT gate," Nature **426**(6964), 264–267 (2003).
45. S. Ecker, P. Sohr, L. Bulla, *et al.*, "Experimental single-copy entanglement distillation," Phys. Rev. Lett. **127**(4), 040506 (2021).
46. X. M. Hu, C. X. Huang, Y. B. Sheng, *et al.*, "Long-distance entanglement purification for quantum communication," Phys. Rev. Lett. **126**(1), 010503 (2021).
47. J. W. Pan, S. Gasparoni, R. Ursin, *et al.*, "Experimental entanglement purification of arbitrary unknown states," Nature **423**(6938), 417–422 (2003).
48. C. H. Bennett, G. Brassard, S. Popescu, *et al.*, "Purification of noisy entanglement and faithful teleportation via noisy channels," Phys. Rev. Lett. **76**(5), 722–725 (1996).
49. C. Vigliar, S. Paesani, Y. Ding, *et al.*, "Error-protected qubits in a silicon photonic chip," Nat. Phys. **17**(10), 1137–1143 (2021).
50. J. C. Adcock, C. Vigliar, R. Santagati, *et al.*, "Programmable four-photon graph states on a silicon chip," Nat. Commun. **10**(1), 3528 (2019).
51. W. B. Gao, P. Xu, X. C. Yao, *et al.*, "Experimental realization of a controlled-NOT gate with four-photon six-qubit cluster states," Phys. Rev. Lett. **104**(2), 020501 (2010).
52. H. J. Briegel, D. E. Browne, W. Dür, *et al.*, "Measurement-based quantum computation," Nat. Phys. **5**(1), 19–26 (2009).
53. G. Vallone, E. Pomarico, F. De Martini, *et al.*, "Active one-way quantum computation with two-photon four-qubit cluster states," Phys. Rev. Lett. **100**(16), 160502 (2008).
54. R. Prevedel, P. Walther, F. Tiefenbacher, *et al.*, "High-speed linear optics quantum computing using active feed-forward," Nature **445**(7123), 65–69 (2007).
55. P. Walther, K. J. Resch, T. Rudolph, *et al.*, "Experimental one-way quantum computing," Nature **434**(7030), 169–176 (2005).

56. L. M. Duan and R. Raussendorf, "Efficient quantum computation with probabilistic quantum gates," Phys. Rev. Lett. **95**(8), 080503 (2005).
57. M. A. Nielsen, "Optical quantum computation using cluster states," Phys. Rev. Lett. **93**(4), 040503 (2004).
58. B. J. Metcalf, J. B. Spring, P. C. Humphreys, *et al.*, "Quantum teleportation on a photonic chip," Nat. Photonics **8**(10), 770–774 (2014).
59. D. Llewellyn, Y. Ding, I. I. Faruque, *et al.*, "Chip-to-chip quantum teleportation and multi-photon entanglement in silicon," Nat. Phys. **16**(2), 148–153 (2020).
60. X. Cheng, K.-C. Chang, Z. Xie, *et al.*, "A chip-scale polarization-spatial-momentum quantum SWAP gate in silicon nanophotonics," Nat. Photonics **17**(8), 656–665 (2023).
61. K.-C. Chang, X. Cheng, M. C. Sarihan, *et al.*, "Recent advances in high-dimensional quantum frequency combs," Newton **1**(1), 100024 (2025).
62. K.-C. Chang, X. Cheng, M. C. Sarihan, *et al.*, "648 Hilbert space dimensionality in a biphoton frequency comb: entanglement formation and Schmidt mode decomposition," npj Quantum Inf. **7**, 48 (2021).
63. H.-H. Lu, J. M. Lukens, M. Alshowkan, *et al.*, "Building a controlled-NOT gate between polarization and frequency," Opt. Quantum **2**(4), 282 (2024).
64. G. Corrielli, A. Crespi, R. Geremia, *et al.*, "Rotated waveplates in integrated waveguide optics," Nat. Commun. **5**, 4249 (2014).
65. J.-P. Li, X. Gu, J. Qin, *et al.*, "Heralded nondestructive quantum entangling gate with single-photon sources," Phys. Rev. Lett. **126**(14), 140501 (2021).
66. X. H. Bao, T. Y. Chen, Q. Zhang, *et al.*, "Optical nondestructive controlled-NOT gate without using entangled photons," Phys. Rev. Lett. **98**(17), 170502 (2007).
67. Z. Zhao, A. N. Zhang, Y. A. Chen, *et al.*, "Experimental demonstration of a nondestructive controlled-NOT quantum gate for two independent photon qubits," Phys. Rev. Lett. **94**(3), 030501 (2005).
68. S. Gasparoni, J. W. Pan, P. Walther, *et al.*, "Realization of a photonic controlled-NOT gate sufficient for quantum computation," Phys. Rev. Lett. **93**(2), 020504 (2004).
69. K. Nemoto and W. J. Munro, "Nearly deterministic linear optical controlled-NOT gate," Phys. Rev. Lett. **93**(25), 250502 (2004).

Supplemental Document

OPTICA QUANTUM

Quantum teleportation of a silicon nanophotonic CNOT gate: supplement

KAI-CHI CHANG,[1,†,*] XIANG CHENG,[1,5,†] FELIX RIBUOT-HIRSCH,[1] MURAT CAN SARIHAN,[1] YUJIE CHEN,[1,6] JAIME GONZALO FLOR FLORES,[1] MINGBIN YU,[2,3] PATRICK GUO-QIANG LO,[2,4] DIM-LEE KWONG,[2] AND CHEE WEI WONG[1,7]

[1]*Fang Lu Mesoscopic Optics and Quantum Electronics Laboratory, Department of Electrical and Computer Engineering, University of California, Los Angeles, California 90095, USA*
[2]*Institute of Microelectronics, Singapore 117685, Singapore*
[3]*State Key Laboratory of Functional Materials for Informatics, Shanghai Institute of Microsystem and Information Technology and Shanghai Industrial Technology Research Institute, Shanghai 200050, China*
[4]*Advanced Micro Foundry, Singapore 117685, Singapore*
[5]*chengxiang@ucla.edu*
[6]*yujiechen0724@ucla.edu*
[7]*cheewei.wong@ucla.edu*
[†]*These authors contributed equally to this work.*
[*]*uclakcchang@ucla.edu*

This supplement published with Optica Publishing Group on 7 August 2025 by The Authors under the terms of the Creative Commons Attribution 4.0 License in the format provided by the authors and unedited. Further distribution of this work must maintain attribution to the author(s) and the published article's title, journal citation, and DOI.

Supplement DOI: https://doi.org/10.6084/m9.figshare.29618648

Parent Article DOI: https://doi.org/10.1364/OPTICAQ.554577

Supplement

Quantum teleportation of a silicon nanophotonic CNOT gate

Kai-Chi Chang[1,†,*], Xiang Cheng[1,†,*], Felix Ribuot-Hirsch[1], Murat Can Sarihan[1], Yujie Chen[1,*], Jaime Gonzalo Flor Flores[1], Mingbin Yu[2,3], Patrick Guo-Qiang Lo[2,4], Dim-Lee Kwong[2], and Chee Wei Wong[1,*]

[1]Fang Lu Mesoscopic Optics and Quantum Electronics Laboratory, Department of Electrical and Computer Engineering, University of California, Los Angeles, CA 90095, USA

[2]Institute of Microelectronics, Singapore 117685, Singapore

[3]State Key Laboratory of Functional Materials for Informatics, Shanghai Institute of Microsystem and Information Technology, and Shanghai Industrial Technology Research Institute, Shanghai 200050, China

[4]Advanced Micro Foundry, Singapore 117685, Singapore

[†] These authors contributed equally to this work.

[*] Corresponding author emails: uclakcchang@ucla.edu, chengxiang@ucla.edu, yujiechen0724@ucla.edu, and cheewei.wong@ucla.edu

S.I. Spectral, temporal, and polarization characterization of our photon-pair source

In Figure S.1, we show the frequency spectrum of our measured spontaneous parametric down-conversion (SPDC) source in this study. We conducted measurements using a telecom-band tunable BPF with a full width at half maximum (FWHM) bandwidth of 0.3 nm. In Figure S.1, we present the measured frequency spectrum of our spontaneous parametric down-conversion (SPDC) source used in this work. The measurements are performed by a telecom-band tunable Gaussian BPF with a full width at half maximum (FWHM) bandwidth of 0.3 nm. Our SPDC source has $\approx$ 0.2 nm center wavelength difference, with signal photon FWHM bandwidth of $\approx$ 295 GHz, and idler photon FWHM bandwidth of $\approx$ 286 GHz. We carefully sweep pump wavelengths and choose this near-degenerate operation point for optimum overlapping of signal and idler frequencies.

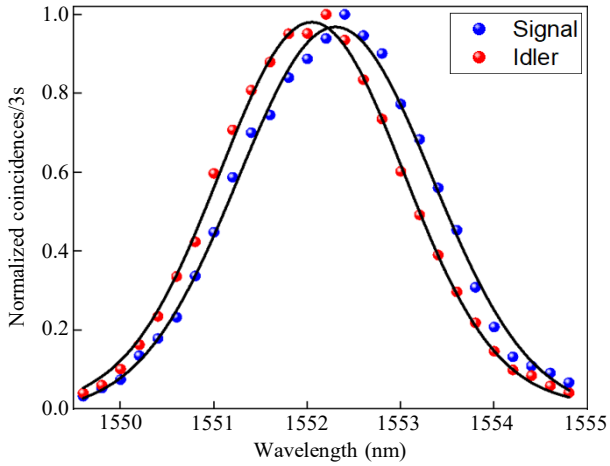

Figure S.1. **Measured frequency spectrum of SPDC photons.** Experimental frequency spectrum of signal and idler photons of photon-pair source used in this work. The measurements are performed by a telecom-band tunable Gaussian BPF with a full width at half maximum (FWHM) bandwidth of 0.3 nm. Our SPDC source has $\approx$ 0.2 nm center wavelength difference, with signal photon FWHM bandwidth of $\approx$ 295 GHz, and idler photon FWHM bandwidth of $\approx$ 286 GHz. We carefully sweep pump wavelengths and choose this near-degenerate operation point for optimum overlapping of signal and idler frequencies.

The Hong-Ou-Mandel (HOM) two-photon interference visibility is mainly determined by spectral, temporal, and polarization indistinguishability between biphotons [S1-S5]. After optimizing spectral indistinguishability between biphotons of our SPDC source, we proceed to perform HOM interference measurement to fully characterize our photon-pair source. The biphotons are divided by a PBS_1 and then sent into a 50:50 fiber BS_1 from different sides (for detail experimental setups, see main text Fig. 1c). To enhance the count rate of biphotons before their separation, we employ a fiber polarization controller (FPC_2). For achieving temporal indistinguishability, we incorporate two tunable delay lines, allowing us to obtain optimal temporal overlap between biphotons. To ensure polarization indistinguishability, we mount a half-wave plate (HWP_1) on the idler photons. This half-wave plate aligns the polarization of biphotons to be the same at the fiber beam splitter (BS_1). Here we use the same notation as the main text for consistency. Figure S.2 illustrates the HOM interference dip. In Figure S.2(a), for our SPDC source, we obtain a HOM visibility of 97.4 (92.2) ± 0.8% after (before) background subtraction. The base-to-base dip width indicates the two-photon coherence time of the SPDC photon pairs,

which is measured to be 3.22 ± 0.02 ps, corresponding to a two-photon bandwidth of 310 ± 2.0 GHz, which is close to the frequency spectrum sweeping measurements in Figure S.1. After confirming that we have a good overlapping of two-photon wavepacket for our SPDC source, we continue to use HOM two-photon interference to check whether the free-space Mach-Zehnder interferometer is balanced. In Figure S.2(b), we obtain a HOM visibility of 97.1 (91.7) ± 0.8% after (before) background subtraction. The base-to-base dip width indicates the two-photon coherence time of the SPDC photon pairs after passing through a balanced Mach-Zehnder interferometer, which is measured to be 3.24 ± 0.02 ps, corresponding to a two-photon bandwidth of 308 ± 2.0 GHz, which matches well with our measurements in Figure S.2(a) and S.1.

Note that for this particular measurements, we use the same bandpass filter (BPF) used directly after PBS_1 to make sure the SPDC frequency is consistent between measurements in Figure S.2(a) and S.2(b) so the temporal delay position can be fixed. The optimum HOM dip position and coincidence count difference between Figure S.2(a) and S.2(b) arises from the different experimental setup used. For HOM interference measurements in Figure S.2, we can always use narrower BPF or decrease the pump power to improve HOM visibility [S6, S7], however, such arrangements will unavoidably lower the photon flux for our on-chip CNOT gate teleportation measurements, hence, here we choose to use relatively high pump power ≈ 12.5 mW throughout all the measurements presented in this work.

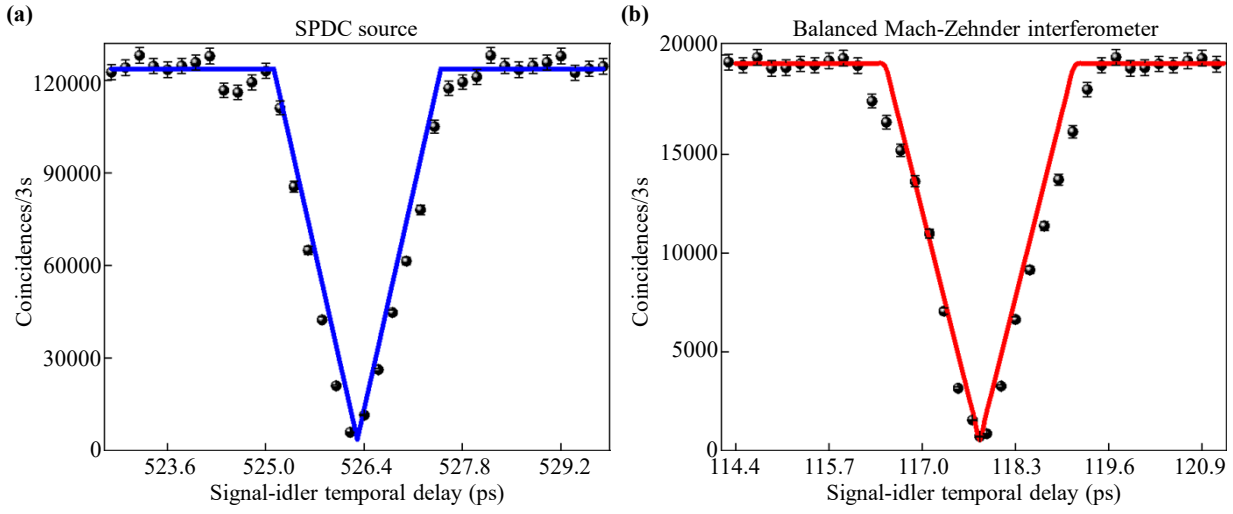

Figure S.2. **Hong-Ou-Mandel two-photon interference dip measurements. (a)** For our SPDC source, we obtain an optimized HOM visibility of 97.4 (92.2) ± 0.8% after (before) background

subtraction. The base-to-base dip width indicates the two-photon coherence time of the SPDC photon pairs, which is measured to be 3.22 ± 0.02 ps, corresponding to a two-photon bandwidth of 310 ± 2.0 GHz, which is close to the frequency spectrum sweeping measurements in Figure S.1. **(b)** We also use HOM two-photon interference to check the free-space Mach-Zehnder interferometer is balanced. In Figure S.2(b), we obtain a HOM visibility of 97.1 (91.7) ± 0.8% after (before) background subtraction. The base-to-base dip width indicates the two-photon coherence time of the SPDC photon pairs after passing through a balanced Mach-Zehnder interferometer, which is measured to be 3.24 ± 0.02 ps, corresponding to a two-photon bandwidth of 308 ± 2.0 GHz, which matches well with our measurements in Figure S.2(b) and S.1.

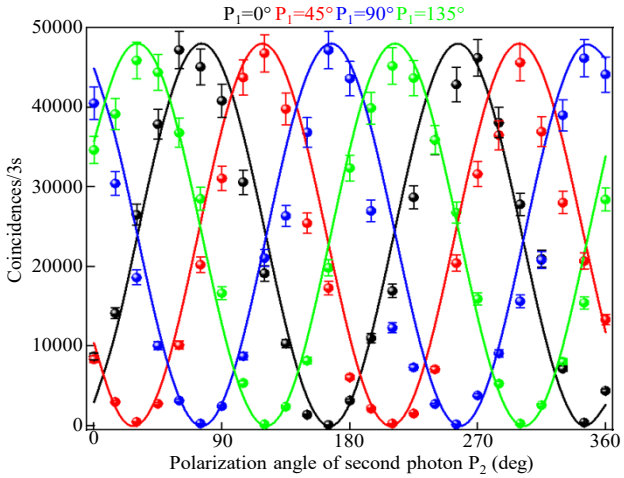

Figure S.3. **Post-selected generated polarization entanglement of SPDC source.** We measure and achieve 98.5 (93.9) ± 1.0% fringe visibility after (before) background subtraction. For polarization fringes after accidental subtraction, we obtain $S = 2.686 \pm 0.033$ to violate the classical limit by more than 20 standard deviations [S8].

Finally, we measure and generate polarization-entanglement after HOM interference measurement by simply rotating the polarization of the idler photons by 90º. In Figure S.3, we present the post-selected polarization entanglement after the fiber BS_1 using standard polarization projection measurements with 98.5 (93.9) ± 1.0% fringe visibility after (before) background subtraction. For polarization fringes after accidental subtraction, we extract a $S = 2.686 \pm 0.033$ to violate the classical limit by more than 20 standard deviations [S8].

S.II. Quantum state tomography after an on-chip CNOT gate teleportation

In this supplementary section, we present the quantum state tomography of other input polarization states after an on-chip CNOT gate teleportation. Here we analyze our on-chip CNOT gate teleportation of the remote qubits 1 and 4 by performing quantum state tomography [S8-S10], given 14 different input states $|00\rangle$, $|01\rangle$, $|0+\rangle$, $|0i\rangle$, $|10\rangle$, $|11\rangle$, $|1+\rangle$, $|1i\rangle$, $|++\rangle$, $|+i\rangle$, $|i0\rangle$, $|i1\rangle$, $|i+\rangle$, and $|ii\rangle$, where $|+\rangle = (|0\rangle + |1\rangle)/\sqrt{2} = |D\rangle$, and $|i\rangle = (|0\rangle + i|1\rangle)/\sqrt{2} = |R\rangle$. The quantum state tomography result for the other two input polarization states $|+0\rangle$, $|+1\rangle$ is given in main text Fig. 3a and 3b. In Figure S.4, we prepare four input polarization states, $|00\rangle$, $|01\rangle$, $|0+\rangle$, $|0i\rangle$, and output polarization states are all 16 states consists of $|0\rangle$, $|1\rangle$, $|+\rangle$, and $|i\rangle$. The density matrix for each output polarization state is reconstructed using a maximum-likelihood algorithm from the measurements [S10-S13]. After successfully reconstructing the density matrix, we can assess the measured state fidelity. The state fidelity quantifies the similarity between the measured state and the ideal state, and it is defined as follows: $F_s = (Tr(\sqrt{\sqrt{\rho_{mea}}\rho_{ideal}\sqrt{\rho_{mea}}}))^2$, where ρ_{ideal} is the ideal density matrix, and ρ_{mea} is the measured density matrix. We reconstruct the teleported two-qubit CNOT gate state tomography and obtain an average quantum state fidelity of 88.9 ± 0.6% for these four input states. In Figure S.5, we present the quantum state tomography results of our teleported on-chip CNOT gate, where we measure and achieve average quantum state fidelity F_s of 88.4 ± 1.0% for $|10\rangle$, $|11\rangle$, $|1+\rangle$, and $|1i\rangle$ input states. Next, in Figure S.6, we prepare $|++\rangle$, $|+i\rangle$ input states and fed them into our non-local CNOT gate. The outputs contain the same output polarization states as those in Figure S.5, and we can retrieve an average quantum state fidelity of 83.4 ± 1.1% for these two input states. Finally, in Figure S.7, we prepare more complex polarization states $|i0\rangle$, $|i1\rangle$, $|i+\rangle$, and $|ii\rangle$ and send them into remote qubits 1 and 4. Output polarization states are the 16 independent polarization states comprised of $|0\rangle$, $|1\rangle$, $|+\rangle$, and $|i\rangle$. We successfully optimize and achieve an average quantum state fidelity of 85.3 ± 2.6% for these four input states. For Figure S.4 to S.7, besides the errors from imperfect experimental non-local truth tables shown in main text Fig. 2c, these quantities include imperfections associated with logical state preparation and decoding operations. The ideal values are indicated as transparent bars in the plots. The duration of coincidence counting for each experimental data in Figure S.4 to S.7 is 10 second, and all the data are obtained without subtracting accidental coincidences. Our quantum state tomography results in Figure S.4 to S.7 are consistent with our non-local truth table, quantum state tomography measurements in main text Fig. 2c, and produced

Bell state measurements in main text Fig. 3, further confirming the non-local gate operation between remote qubit 1 and 4 using our teleported chip-scale CNOT gate.

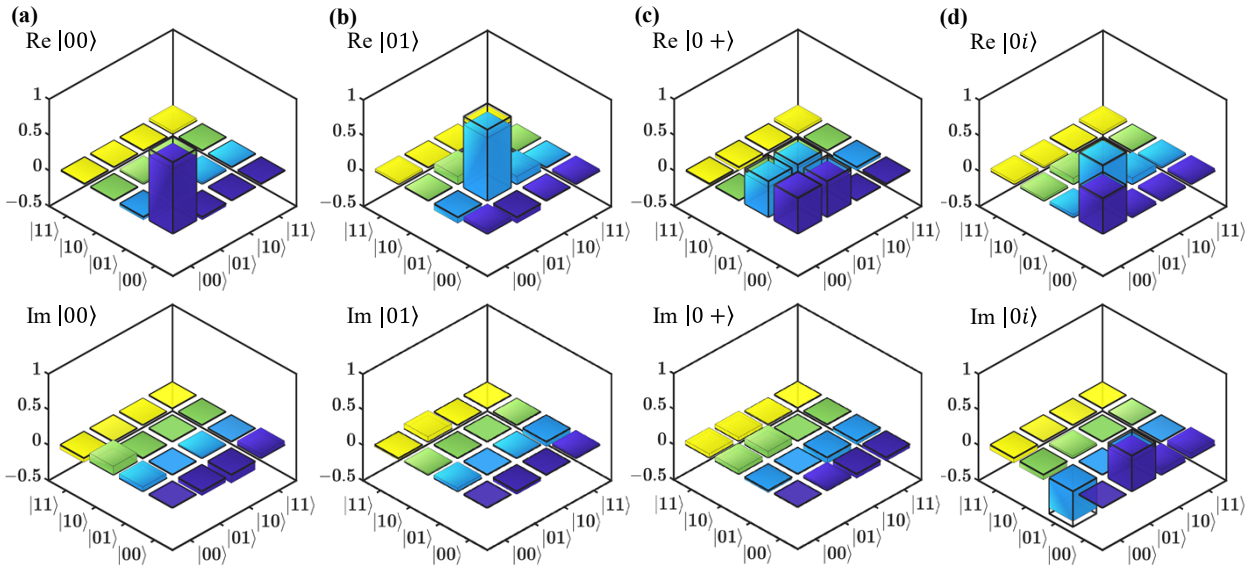

Figure S.4. **Teleported quantum state tomography of an on-chip CNOT gate teleportation with $|00\rangle$, $|01\rangle$, $|0+\rangle$, and $|0i\rangle$ input states. (a)** to **(d),** Teleported quantum state tomography of an on-chip CNOT gate for input polarization states of $|00\rangle$, $|01\rangle$, $|0+\rangle$, and $|0i\rangle$, respectively. The real and imaginary part of density matrices are reconstructed by using 16 different output polarization settings, $|00\rangle$, $|01\rangle$, $|0+\rangle$, $|0i\rangle$, $|10\rangle$, $|11\rangle$, $|1+\rangle$, $|1i\rangle$, $|+0\rangle$, $|+1\rangle$, $|++\rangle$, $|+i\rangle$, $|i0\rangle$, $|i1\rangle$, $|i+\rangle$, and $|ii\rangle$. We measure and obtain an average quantum state fidelity of $88.9 \pm 0.6\%$ for these four input states. The ideal values are indicated as transparent bars in the plots.

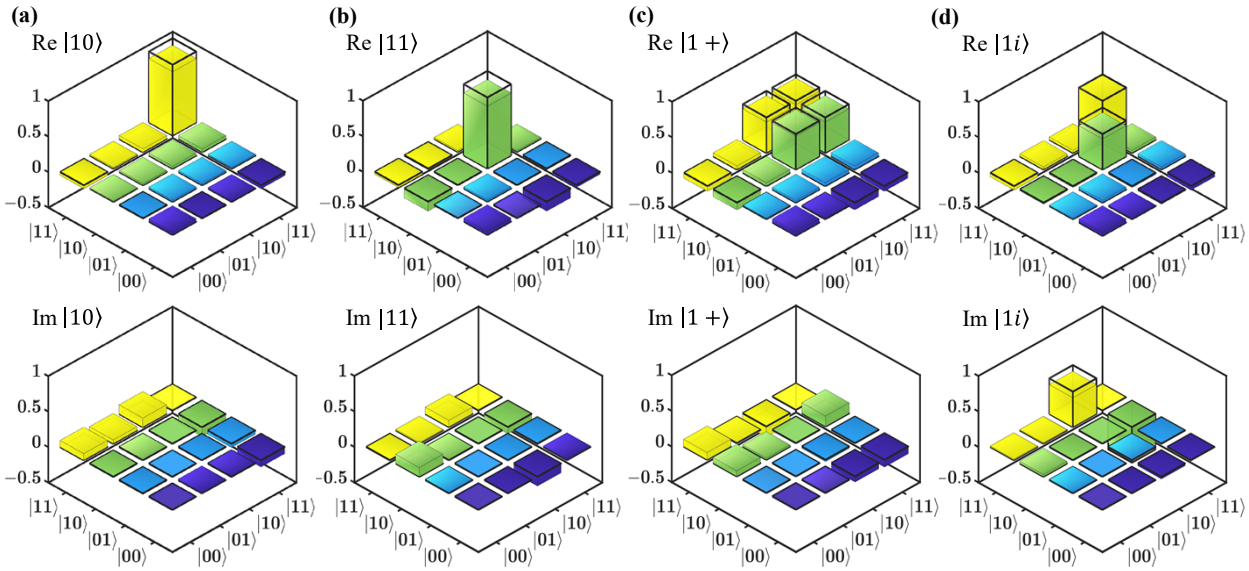

Figure S.5. **Quantum state tomography after a chip-scale CNOT gate teleportation with $|10\rangle$, $|11\rangle$, $|1+\rangle$, and $|1i\rangle$ input states. (a)** to **(d),** Teleported quantum state tomography of an on-chip CNOT gate for input polarization states of $|10\rangle$, $|11\rangle$, $|1+\rangle$, and $|1i\rangle$, respectively. The real and imaginary part of density matrices are reconstructed by using 16 different output polarization settings, $|00\rangle$, $|01\rangle$, $|0+\rangle$, $|0i\rangle$, $|10\rangle$, $|11\rangle$, $|1+\rangle$, $|1i\rangle$, $|+0\rangle$, $|+1\rangle$, $|++\rangle$, $|+i\rangle$, $|i0\rangle$, $|i1\rangle$, $|i+\rangle$, and $|ii\rangle$. We measure and obtain an average quantum state fidelity of 88.4 ± 1.0% for these four input states. The ideal values are indicated as transparent bars in the plots.

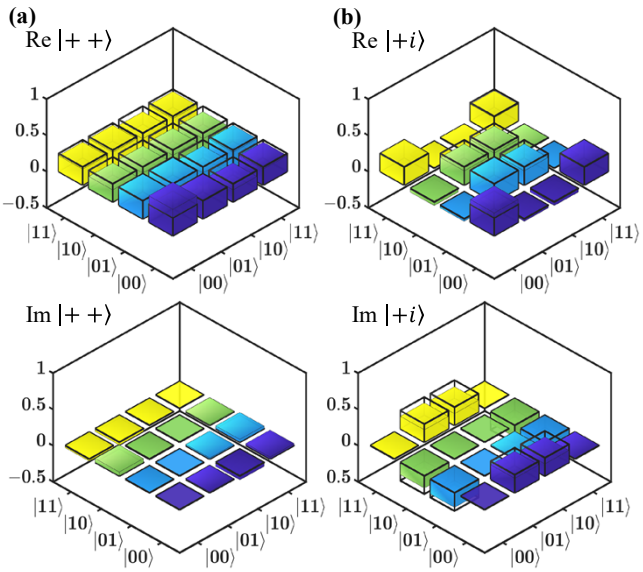

Figure S.6. **Teleported quantum state tomography of a chip-scale CNOT gate with $|++\rangle$, and $|+i\rangle$ input states. (a)** and **(b),** Teleported quantum state tomography of an on-chip CNOT gate for input polarization states of $|++\rangle$, and $|+i\rangle$, respectively. The real and imaginary part of density matrices are reconstructed by using 16 different output combinations of $|0\rangle$, $|1\rangle$, $|+\rangle$, and $|i\rangle$. We measure an average quantum state fidelity of 83.4 ± 1.1% for these two input states. The ideal values are indicated as transparent bars in the plots.

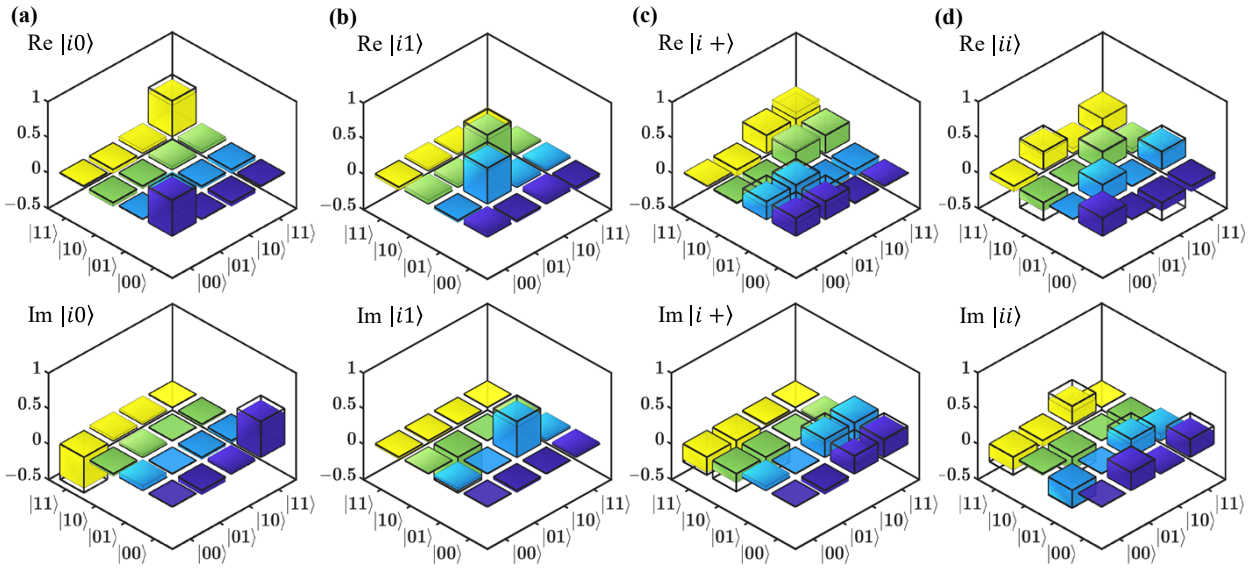

Figure S.7. **Quantum state tomography after a chip-scale CNOT gate teleportation with $|i0\rangle$, $|i1\rangle$, $|i+\rangle$, and $|ii\rangle$ input states. (a)** to **(d),** Teleported quantum state tomography of an on-chip CNOT gate for input polarization states of $|i0\rangle$, $|i1\rangle$, $|i+\rangle$, and $|ii\rangle$, respectively. The real and imaginary part of density matrices are reconstructed by using 16 different output polarization settings, $|00\rangle$, $|01\rangle$, $|0+\rangle$, $|0i\rangle$, $|10\rangle$, $|11\rangle$, $|1+\rangle$, $|1i\rangle$, $|+0\rangle$, $|+1\rangle$, $|++\rangle$, $|+i\rangle$, $|i0\rangle$, $|i1\rangle$, $|i+\rangle$, and $|ii\rangle$. We optimize and measure an average quantum state fidelity of 85.3 ± 2.6% for these four input states. The ideal values are indicated as transparent bars in the plots.

Methods

Chip nanofabrication

Our on-chip CNOT gate is a silicon waveguide device realized by a polarization directional coupler [S8]. The waveguide-to-waveguide gap width and coupling length for our silicon CNOT gate has been optimized to be 400 nm and 11.5 μm, respectively. A 2 μm SiO_2 cladding is

deposited on top of the core by high-density plasma-enhanced chemical vapor deposition. For photon input-output coupling, our standardized design library with inverse adiabatic couplers is implemented. This consists of a silicon nano-tip of ≈ 180 nm, with mode evolving to the standardized single-mode width. The SiO_2 cladding on the nano-tip forms an oxide waveguide, with air-trenches on the lateral transverse sides of the oxide waveguide. The input and output facets of the device are formed through the process of deep reactive-ion etching. The CNOT gate only require silicon and silicon oxide interfaces, which are compatible in silicon foundries.

Experimental details

We use a continuous-wave distributed Bragg reflector single-frequency laser (Photodigm PH776DBR) to pump a type-II periodically-poled potassium titanyl phosphate (PPKTP) waveguide (AdvR Inc.) at 1552 nm. The fiber polarization controller (FPC_1) before the PPKTP waveguide is used to maximize the generation of orthogonally-polarized SPDC photons. To enhance the coincidence counts after the separation of two photons, FPC_2 is employed for optimization purposes. To eliminate pump photons, a long-pass filter (LPF) and a rotatable band-pass filter (BPF) (Semrock NIR01-1570/3) are utilized. Then, we use a polarizing beam splitter (PBS_1) to separate signal and idler photons and feed them to Alice and Bob. The polarization-entangled states for on-chip CNOT gate teleportation are prepared by post-selection. We first combine signal and idler photons through a 50:50 fiber beam splitter (BS_1) while ensuring they have orthogonal polarizations. To achieve picosecond level temporal indistinguishability between biphotons, we carefully tune their relative delay with two motorized tunable delay lines (Luna Innovations MDL-002). This leads to the HOM dip, after which we tune idler photons' polarization by 90º for generation of polarization entanglement with post-selection. This polarization entanglement is confirmed after the fiber BS_1 using standard polarization projection measurements. The HOM dip measurements and post-selected polarization entanglement are presented in Supplementary Materials Section I. We then use fiber PBS_2 and PBS_3 to convert polarization qubits to path qubits for Alice and Bob. We insert another FPC (not shown) before fiber PBS_2 to maintain polarizations of input states. On Alice side, we use FPC_3 and FPC_4 to make sure the polarization state is $|H\rangle$ before local gate operation, then we send both inputs into our two-qubit on-chip CNOT gate device. We insert a pair of half-wave plates and quarter-wave plates (HWP_2, QWP_1, HWP_3, QWP_2) on both input ports before the chip to prepare arbitrary input polarization states between qubits 1 and 2 from Alice. In Bob's side, HWP_6 is placed before PBS_3 to

compensate the small polarization variation in a short fiber after polarization-entanglement generation from the fiber BS_1. HWP_4 is rotated to 45º to convert polarization $|V\rangle$ to $|H\rangle$, and HWP_7, QWP_3, HWP_8, QWP_4 are used for preparing different polarization states before the Bob's CNOT gate.

Next we proceed to prepare Alice and Bob's CNOT gates. For Alice's CNOT gate, we fix our nanofabricated silicon chip device on a custom-build chip holder, with temperature stability of ≈ 1 mK temperature for 24 hours. We build a dual-input-output free-space coupling system to fully access available Hilbert space dimensionality of our on-chip CNOT gate, and the optimized coupling loss for this setup is ≈ 10 dB per channel. After collecting output photons from our silicon chip, we send the photons to two fiber benches, with polarization analyzers (HWP_9, QWP_5, P_1, HWP_{10}, QWP_6, P_2) mounted for polarization projection measurements on qubits 1 and 2. Second, we construct a free-space setup on Bob's side, the HWP_5 is rotated to 45º to act as Bob's CNOT gate. We use FPC_5 and FPC_6 to compensate the polarization drift of two motorized tunable fiber delay lines. Then, to erase which-path information and to match temporal wavepackets after free-space CNOT gate, we connect both outputs of Bob's qubits into 50:50 fiber BS_2. Finally, we send the output photons from fiber BS_2 into the other two fiber benches, with polarization analyzers (HWP_{11}, QWP_7, P_3, HWP_{12}, QWP_8, P_4) mounted for polarization projection measurements on qubits 3 and 4. Both Alice and Bob's CNOT gates truth table measurements are given in main text Fig. 2a and 2b. Here we use the same notation for experimental optical components as the main text for consistency.

After preparing polarization-entangled photon-pair source, Alice and Bob's CNOT gates, we carefully tape down all the fiber components, and send our polarization-entangled source to these two spatially separated experimental setups for implementing quantum gate teleportation via our on-chip CNOT gate. Based on different measurements performed in this work, we prepare input polarization states consists of $|H\rangle$, $|V\rangle$, $|D\rangle$, and $|R\rangle$ (or $|0\rangle$, $|1\rangle$, $|+\rangle$, and $|i\rangle$) between remote qubits 1 and 4. Then, we use polarization analyzers for these non-local qubits to measure the coincidence counts with time-correlated single-photon counting (TCSPC) module (Picoharp 300) to implement our on-chip CNOT quantum gate teleportation.

Quantum state and process tomography

Quantum state tomography serves the purpose of reconstructing an unknown quantum state in its entirety with corresponding measurements [S9]. Achieving reliable quantum state tomography

relies on minimizing errors in both state preparation and measurement processes. The quantum state fidelity can be expressed as: $F_s = (Tr(\sqrt{\sqrt{\rho_{mea}}\rho_{ideal}\sqrt{\rho_{mea}}}))^2$, where ρ_{mea}, ρ_{ideal} is the measured and ideal density matrix, respectively. This fidelity quantifies the level of agreement between the ideal polarization states and the polarization states that are actually measured. The method of quantum process tomography was proposed as a way to fully characterize a quantum process [S14]. Quantum process tomography enables the complete experimental reconstruction of any quantum process through the representation of a χ matrix [S15]. Quantum process tomography is able to determine the effects of a "black box" quantum operation on *N* qubits by characterizing the gate's operation. For two-qubit process tomography of our teleported on-chip CNOT gate, we select operator basis $\tilde{E} = \sigma_m \otimes \sigma_n$, where $m, n = I, X, Y, Z$. We prepare 16 different polarization input states that consist of $|H\rangle$, $|V\rangle$, $|D\rangle$, and $|R\rangle$ (or $|0\rangle$, $|1\rangle$, $|+\rangle$, and $|i\rangle$), respectively. The output states after non-local CNOT gate operation are then measured in the same basis with density matrices reconstructed via quantum state tomography. The reconstructed density matrices and process matrices might be non-physical due to the noise in the measurement process. Hence, we utilize the maximum-likelihood estimation for both quantum state and process tomography to find the closest matrix to the measured one [S15]. The fidelity of a quantum process can be defined as follows: $F_p = (Tr(\sqrt{\sqrt{\chi_{exp}}\chi_{ideal}\sqrt{\chi_{exp}}}))^2$, where χ_{exp}, χ_{ideal} is the experimental and the ideal process matrix, respectively. Given that we have the experimental quantum process fidelity F_p, we can obtain the average gate fidelity by $F_{avg} = (dF_p + 1)/(d + 1)$. Since the Hilbert space dimensionality of a CNOT gate is $d = 4$, we can extract experimental average gate fidelity after our on-chip CNOT gate teleportation.

Supplementary References

[S1] Y. J. Lu, R. L. Campbell, and Z. Y. Ou, Mode-locked two-photon states, *Phys. Rev. Lett.* **91**, 163602 (2003).

[S2] T. Gerrits, F. Marsili, V. B. Verma, L. K. Shalm, M. Shaw, R. P. Mirin, and S. W. Nam, Spectral correlation measurements at the Hong-Ou-Mandel interference dip, *Phys. Rev. A* **91**, 013830 (2015).

[S3] C. Chen, J. E. Heyes, K. H. Hong, M. Y. Niu, A. E. Lita, T. Gerrits, S. W. Nam, J. H. Shapiro, and F. N. C. Wong, Indistinguishable single-mode photons from spectrally engineered biphotons, *Opt. Express* **27**, 11626 (2019).

[S4] K.-C. Chang, X. Cheng, M. C. Sarihan, A. V. Kumar, Y. S. Lee, T. Zhong, Y.-X. Gong, Z. Xie, J. H. Shapiro, F. N. C. Wong, and C. W. Wong, 648 Hilbert Space Dimensionality in a Biphoton Frequency Comb: entanglement formation and Schmidt mode decomposition, *npj Quan. Inf.* **7**, 48 (2021).
[S5] T. Zhong, F. N. C. Wong, T. D. Roberts, and P. Battle, High performance photon- pair source based on a fiber-coupled periodically poled KTiOPO4 waveguide, *Opt. Express* **17**, 12019 (2009).
[S6] X. Xu, Z. Xie, J. Zheng, J. Liang, T. Zhong, M. Yu, S. Kocaman, G.-Q. Lo, D.-L. Kwong, D.R. Englund, F. N. C. Wong, and C. W. Wong, Near-infrared Hong-Ou-Mandel interference on a silicon quantum photonic chip, *Opt. Express* **21**, 5014 (2013).
[S7] T. Kim, M. Fiorentino, and F. N. C. Wong, Phase-stable source of polarization-entangled photons using a polarization Sagnac interferometer, *Phys. Rev. A* **73,** 012316 (2006).
[S8] X. Cheng, K.-C. Chang, Z. Xie, M. C. Sarihan, Y. S. Lee, Y. Li, X. Xu, A. V. Kumar, S. Kocaman, M. Yu, P. G.-Q. Lo, D.-L. Kwong, J. H. Shapiro, F. N. C. Wong, and C. W. Wong, A chip-scale polarization-spatial-momentum quantum SWAP gate in silicon nanophotonics, *Nat. Photon.* **17**, 656 (2023).
[S9] D. F. James, P. G. Kwiat, W. J. Munro, and A. G. White, Measurement of qubits, *Phys. Rev. A* **64**, 052312 (2001).
[S10] J. B. Altepeter, E. R. Jeffrey, and P. G. Kwiat, Photonic state tomography, *Adv. At. Mol. Opt. Phys.* **52**, 105 (2005).
[S11] J. Fiurášek, Maximum-likelihood estimation of quantum measurement, *Phys. Rev. A* **64**, 024102 (2001).
[S12] J. B. Altepeter, D. Branning, E. Jeffrey, T. C. Wei, P. G. Kwiat, R. T. Thew, J. L. O'Brien, M. A. Nielsen, and A. G. White, Ancilla-assisted quantum process tomography, *Phys. Rev. Lett.* **90**, 193601 (2003).
[S13] J. Řeháček, Z. Hradil, E. Knill, and A. I. Lvovsky, Diluted maximum-likelihood algorithm for quantum tomography, *Phys. Rev. A* **75**, 042108 (2007).
[S14] J. L. O'Brien, G. J. Pryde, A. Gilchrist, D. F. James, N. K. Langford, T. C. Ralph, and A. G. White, Quantum process tomography of a controlled-NOT gate, *Phys. Rev. Lett.* **93**, 080502 (2004).
[S15] A. G. White, A. Gilchrist, G. J. Pryde, J. L. O'Brien, M. J. Bremner, and N. K. Langford, Measuring two-qubit gates. *J. Opt. Soc. Am. B* **24**, 172 (2007).